Article

Electronically configurable microscopic metasheet robots

🔴 Check for updates

Qingkun Liu [1,8,9], Wei Wang [1,2,9], Himani Sinhmar [2], Itay Griniasty [1],
Jason Z. Kim [1], Jacob T. Pelster[2], Paragkumar Chaudhari[3], Michael F. Reynolds[1],
Michael C. Cao[4], David A. Muller [4], Alyssa B. Apsel [3], Nicholas L. Abbott[5],
Hadas Kress-Gazit[2], Paul L. McEuen [1,6,7] & Itai Cohen [1,6,7] ✉

Shape morphing is vital to locomotion in microscopic organisms but has been challenging to achieve in sub-millimetre robots. By overcoming obstacles associated with miniaturization, we demonstrate microscopic electronically configurable morphing metasheet robots. These metabots expand locally using a kirigami structure spanning five decades in length, from 10 nm electrochemically actuated hinges to 100 μm splaying panels making up the ~1 mm robot. The panels are organized into unit cells that can expand and contract by 40% within 100 ms. These units are tiled to create metasheets with over 200 hinges and independent electronically actuating regions that enable the robot to switch between multiple target geometries with distinct curvature distributions. By electronically actuating independent regions with prescribed phase delays, we generate locomotory gaits. These results advance a metamaterial paradigm for microscopic, continuum, compliant, programmable robots and pave the way to a broad spectrum of applications, including reconfigurable micromachines, tunable optical metasurfaces and miniaturized biomedical devices.

Building microscopic robots with the remarkable shape-shifting and locomotory strategies found in the animal kingdom[1–3] requires development of new platforms. A powerful strategy for replicating such behaviours is to enable shape change through manipulation of Gaussian curvatures via local expansion or contraction of surfaces[4–8]. Recently, there has been tremendous activity in developing responsive materials for such platforms[9–14]. For example, pioneering studies have shown how to develop soft materials that locally expand and contract, including hydrogels, responsive polymers and liquid crystal elastomers that respond to stimuli including temperature, pH, light and magnetic fields[8,15–17]. While the shape-shifting capabilities of these materials are promising, it remains challenging to integrate them with

electronics for local on-board control. Another promising technology is electrochemical actuators, which were used to build electronically integrated microscopic robots[9,18], robotic ciliated metasurfaces[19,20] and self-folding origamis[21]. Devices built from these actuators, however, typically have limited degrees of freedom, and can only adopt a small range of shape conformations. One possible solution for achieving greater shape flexibility is to use such actuators to construct active mechanical metamaterials. Mechanical metamaterials that consist of tessellated building blocks allow multiple degrees of freedom and extraordinary engineered properties[22–24]. Recent pioneering studies have even shown how to make metamaterials with electrical reconfigurability at the microscopic scale[21,25]. Though these structures remain

[1]Laboratory of Atomic and Solid State Physics, Cornell University, Ithaca, NY, USA. [2]Sibley School of Mechanical and Aerospace Engineering, Cornell University, Ithaca, NY, USA. [3]Electrical and Computer Engineering, Cornell University, Ithaca, NY, USA. [4]School of Applied and Engineering Physics, Cornell University, Ithaca, NY, USA. [5]Smith School of Chemical and Biomolecular Engineering, Cornell University, Ithaca, NY, USA. [6]Department of Physics, Cornell University, Ithaca, NY, USA. [7]Kavli Institute at Cornell for Nanoscale Science, Cornell University, Ithaca, NY, USA. [8]Present address: National Key Laboratory of Advanced Micro and Nano Manufacture Technology, Shanghai Jiao Tong University, Shanghai, China. [9]These authors contributed equally: Qingkun Liu, Wei Wang. ✉e-mail: itai.cohen@cornell.edu

limited in their shape transformation and do not locomote, they suggest that one pathway for obtaining microscopic robots with programmable shapes and locomotory mechanisms is to develop novel metamaterial platforms whose cellular structures enable large shape deformations, can be programmed in both spatial and temporal domains, and readily interface with electronics.

Design and fabrication of metasheet robots

Here we implement this approach and create an electronically driven microscale metasheet robot (metabot) platform that, through independent actuation of different local regions with over 200 hinges, can achieve multiple shape transformations and even locomotion. Our metabot design is comprised of a kirigami structure with four levels (Fig. 1a): (1) atomically thin surface electrochemical actuators (SEAs)[9,21] that bend and flatten reversibly to make up micrometre-scale hinges; (2) microsplay origami linkages created from these hinges that convert out-of-plane bending into rotations that splay attached panels; (3) a unit cell created by fabricating a ring of panels and linkages that can radially expand and contract; and (4) millimetre-scale metasheets created by tiling these units together that can adopt various shapes. The technology driving hinge bending is recently developed SEAs, which consist of a 7-nm-thick platinum film capped on one side by a 2-nm-thick titanium film as the passive layer (Fig. 1a; see Methods and Supplementary Fig. 1 for the fabrication process). These actuators are driven by electrochemical redox reactions of the exposed platinum surface[9,21]. Oxidizing the platinum at ~1 V relative to the Ag/AgCl reference electrode causes the exposed platinum surface to expand and the hinge to bend (Fig. 1a, red reaction pathway, top to bottom), while reducing the platinum oxide at −0.5 V returns the actuator to its original state set by prestress generated during fabrication (Fig. 1a, blue reaction pathway, bottom to top). At the next level, we adopt a microsplay linkage[26] that contains two small linkage panels with one mountain (downward) hinge in the centre and two valley (upward) hinges on either side[27–29]. The bending direction is dictated by alternating the growth order of the Pt and Ti layers (Fig. 1b). Here, we design the bending angle of the central mountain hinge to be twice that of the valley hinges so that panels connected by the linkage are planar in the unfolded or fully folded states corresponding to the closed and splayed configurations respectively. By fabricating six panels and linkages in a hexagonal ring, we create a unit cell that radially expands and contracts when the linkages are splayed and closed respectively (Fig. 1c). Finally, these unit cells are tiled to form a metabot sheet that can adopt various shapes depending on which linkages are activated (Fig. 1d).

We fabricate a metasheet with 96 panels as shown by the optical microscopy image in Fig. 1e. We show an annular dark-field scanning transmission electron microscopy image of a fabricated SEA cross-section in Fig. 1f. Shown is a 7-nm-thick Pt film capped on one side by a 2-nm-thick Ti film. A false-coloured scanning electron microscopy (SEM) image of the microsplay origami linkage in the fully folded state is shown in Fig. 1g. Finally, we show a false-coloured SEM image of a portion of the metasheet tiling in the expanded state (Fig. 1h). Because the metasheet is fabricated using photolithographic techniques, we can make millimetre-sized sheets with thousands of building blocks (Fig. 1i).

To demonstrate that these sheets can adopt a wide variety of shapes, we release the fabricated structures and use them to conformally wrap a topographically varied surface or fold under their own weight. Specifically, we wrap a metasheet around a portion of the arm and body of the Statue of Liberty on a US quarter dollar as shown via SEM in Fig. 1j and Supplementary Fig. 3. We find that the sheet is easily able to adapt its shape to the surface contours. Second, we show a metasheet adopting a variety of folds and kinks generated by the flows produced during critical-point drying (Fig. 1k). This flexibility arises from the metasheet's capacity to locally expand or contract the effective area of each unit cell and the ability to link these unit cells together without ripping the sheet apart.

Mechanism of active 3D shape formation

By selectively controlling the expansion of each unit cell, it is possible to program the resulting metasheet shape. To characterize this areal expansion, we fabricate an individual unit cell and determine how its effective area changes with voltage (Fig. 2a, Supplementary Fig. 4 and Supplementary Video 1). In the reduced state, under an applied voltage of −0.5 V, the linkages are fully folded, and the unit cell is in an open configuration. As the voltage relative to the Ag/AgCl reference electrode is increased and the Pt is oxidized, the linkages flatten. We find that for intermediate voltages the unit cell opens further before contracting and reaching a closed state at a voltage of ~1 V. Owing to hysteresis in the SEA actuators, the transition back to an open state occurs over a narrower range of voltages. To quantify these observations, we define the areal expansion ratio, λ, as the projected area encompassed by the panel centres in an actuated unit cell divided by the area of a fully closed unit cell. In the reduced state where the linkage is fully folded, $\lambda = 1.2$. During oxidation the areal expansion reaches a maximum value of $\lambda_{max} = 1.4$, and then decreases to $\lambda_{min} = 1.0$ at ~1 V when the linkage is flat (Fig. 2b, top). These measurements are consistent with the measured cyclic voltammogram for this unit cell, which indicates a large separation between the oxidation and reduction peaks (Fig. 2b, bottom).

To determine how rapidly and robustly the unit cell can switch between states we abruptly change the voltage back and forth from 1 V to −0.5 V. We find that the switching time in both directions is ~100 ms (Fig. 2c), corresponding to a maximum actuation frequency of ~5 Hz. This timescale of switching is determined by both the speed of the redox reaction on platinum driving the microactuator and viscous forces from the fluid, as shown in our previous studies[9,21]. This switching between open and closed states was sustained over hundreds of cycles. The metabot could work in a variety of environments due to the robust electrochemical actuation mechanism. It can work in aqueous solution with a wide pH value range from 0.5 to 13, as well as in biocompatible electrolyte PBS solution[19,21]. On the basis of the Nernst equation, the temperature could shift the driving voltage. Such effects have been discussed in the literature and are not expected to prevent the operation of these metabots[30,31]. The microactuators working in the oxidation–reduction region can cycle >10³ times. The failure mechanism of the metabot is the electrochemical corrosion of platinum in the microactuator[21]. To further improve the durability, we could also actuate using adsorption–desorption of OH⁻ on the surface of platinum rather than oxidation–reduction[9]. This absorption–desorption mechanism could avoid the structural deterioration of the electrodes in pseudocapacitance systems, and has been shown to enable 10⁵ actuation cycles without decay of actuation magnitude[9]. The panel sizes can range from 37.5 μm to 100 μm (Supplementary Fig. 6 and Supplementary Video 3). The lower bound of the panel size is set by the bending radius of the active hinge, while the upper bound depends on the gravitational force in the current version. In the future, we expect that a stronger hinge could lift larger panels and enable higher actuation frequencies. Finally, these unit cells can be tiled together to form a metasheet that can radially expand and contract its area by 40% (Supplementary Fig. 5 and Supplementary Video 2).

Variations in the areal expansion can be used to generate Gaussian curvature as the sheet transitions from the 2D plane to a surface in 3D (Fig. 2d). A simple way to generate a non-uniform areal expansion is to actuate the entire sheet uniformly while tethering the sheet's boundary to the substrate. To demonstrate this simple approach, we fabricated such metasheets, imaged their conformation via confocal microscopy and analysed their shape as described in Methods (Fig. 2e–h and Supplementary Video 4). We found that metabots with square tessellation could not actuate when the boundary was fixed owing to the limited number of degrees of freedom (Supplementary Fig. 7 and
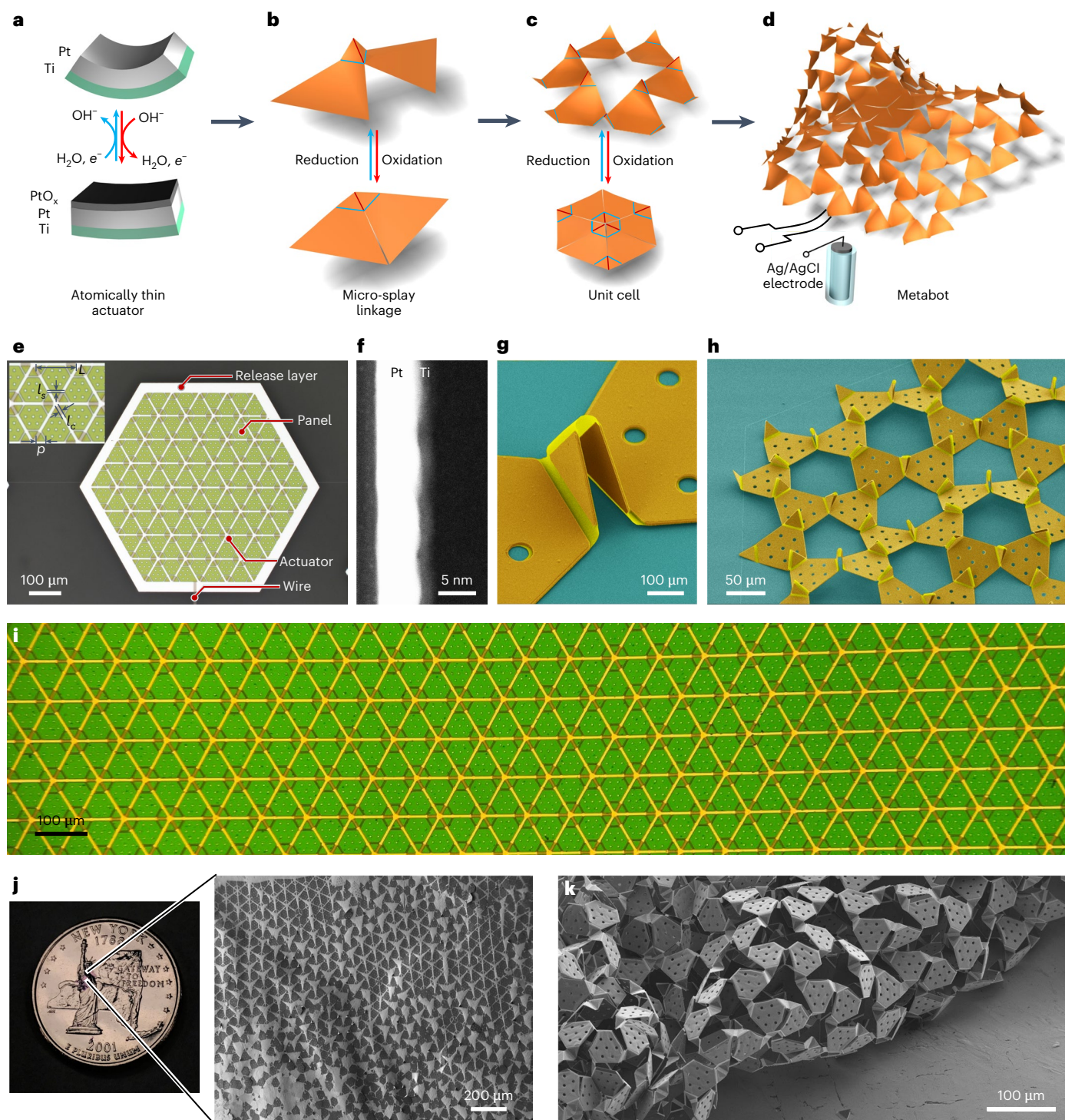
Fig. 1 | Kirigami structure of metabots. a, Redox reactions drive bending in an atomically thin SEA made of a platinum strip capped on one side by a titanium film. **b**, Microsplay origami linkage that converts the out-of-plane bending of SEAs into panel splay. **c**, A unit cell whose area actively expands and contracts under actuation. **d**, A metabot sheet capable of adopting a variety of shapes on the basis of which unit cells are electrically activated. Two lead wires are connected to one panel of the metasheet and the electrical signal is spread throughout the structure via hinges and panels. **e**, An optical microscopy image of a metabot with 96 panels. The lengths of the central hinge l_c and the side hinge l_s are 6 μm and 3 μm, respectively. The lateral length of the triangular building block L is 80 μm while the length of the small triangular panel p is

20 μm. **f**, A scanning transmission electron microscopy image of an actuator cross-section showing the platinum and titanium. **g**, A false-coloured SEM image of a microsplay hinge. Here, the SEAs appear bright yellow and the panels are coloured orange. **h**, A false-coloured SEM image of a metabot sheet. Holes on panels are used to provide etchants access to the sacrificial layer to enable rapid release. **i**, An optical image of a millimetre-scale metabot sheet. **j**, An optical image showing a millimetre-scale metasheet placed on a US quarter dollar coin. The expanded region shows an SEM image of the metabot that has conformally adopted its shape to the contours of the body of the Statue of Liberty displayed on the coin. **k**, An SEM image of a metasheet adopting a variety of folds and kinks generated under critical-point drying.
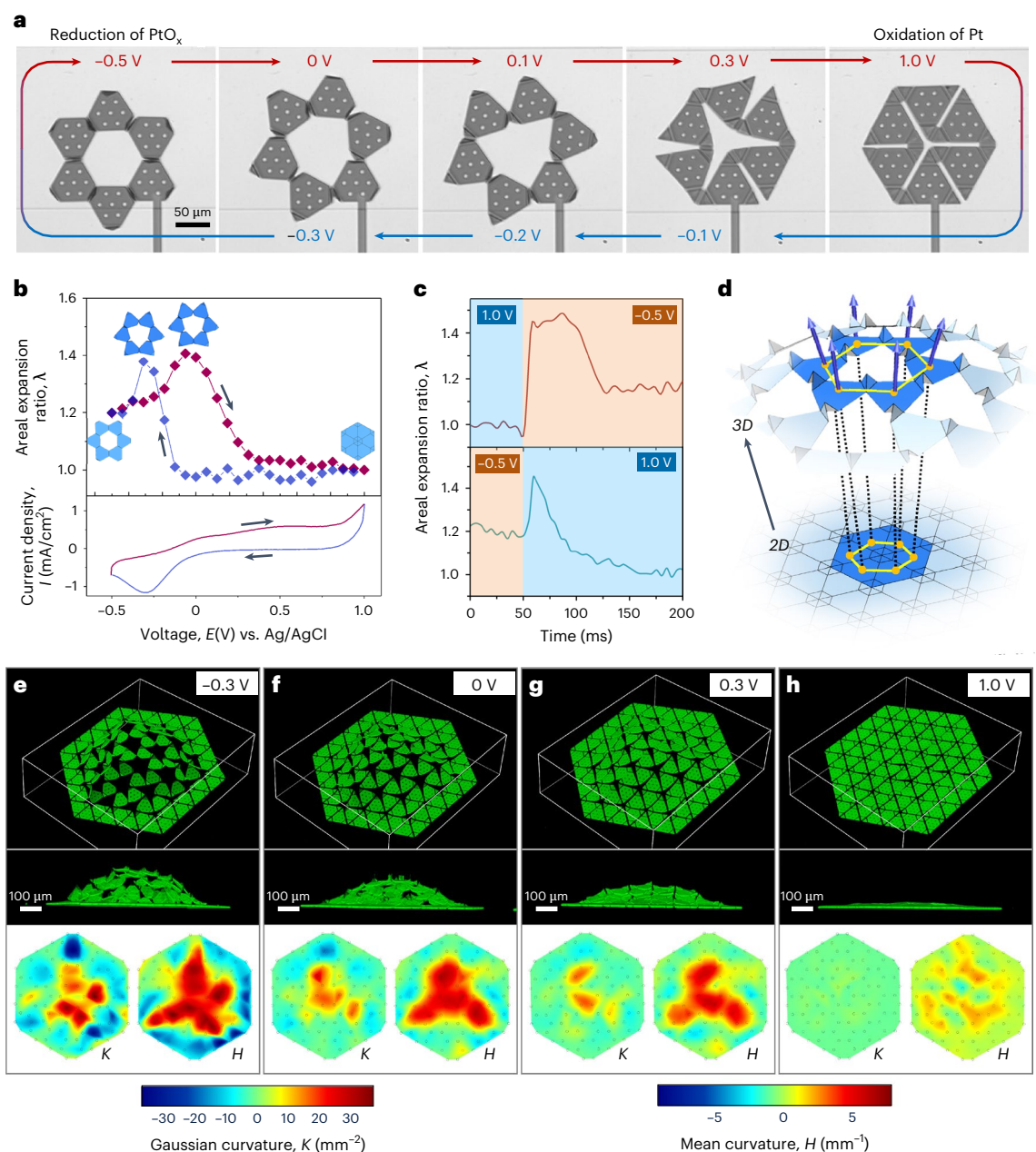
Fig. 2 | Active 3D shape formation. a, Response of a metabot unit cell over a full oxidation (red) and reduction (blue) cycle. **b**, Areal expansion ratio of the unit cell (top) and cyclic voltammetry (bottom) versus applied voltage (relative to a reference electrode). **c**, Change in areal expansion ratio over time during application of a step voltage shows that a unit cell opens and closes in ~100 ms. **d**, Schematic mapping of a 2D fabricated pattern onto a 3D surface under non-uniform areal expansion of the unit cells. **e**–**h**, Confocal microscopy image reconstruction of a fabricated metabot whose periphery is bound to the substrate. Shown are top angle and side images under application of −0.3 V, 0 V, 0.3 V and 1.0 V. The corresponding measured Gaussian (K) and mean (H) curvatures are plotted below each set of images.

Supplementary Video 5). Conversely, in the hexagonal tessellation, when the voltage was swept from +1 V to −0.3 V the sheet opened and buckled into a dome, which retained its configuration when the voltage was removed. Over this range of voltages, the maximum Gaussian curvature (Fig. 2e–h, bottom left) varied from 30 mm^{-2} when the sheet was maximally expanded to 0.3 mm^{-2} when the sheet was in the nearly flat state. We also characterized the mean curvature (Fig. 2e–h, bottom right) of the sheet, which ranged from 7 mm^{-1} when the sheet was maximally expanded to 0.5 mm^{-1} when the sheet was in the nearly flat state.

Electrically programmable 3D shape shifting

Further control over conformation was achieved by fabricating sheets with free boundaries and separately actuating different metasheet

regions. To generate such devices, we fabricated Pt wires that conduct electrical current through the microsplay linkage to reach regions deeper in the metasheet as shown schematically in Fig. 3a and Supplementary Fig. 8. Simulations of the currents through these Pt wires and actuating hinges showed that current crosstalk between these structures was negligible (Supplementary Fig. 9 and Supplementary Video 6). An optical micrograph of a metasheet divided into interior and exterior regions with separate control wires is shown in Fig. 3b. To gain insight into and parametrize the various shapes that could be achieved with this design, we used the Unity3D engine to simulate the actuated sheet and calculate the total elastic energy stored in the hinges (Methods and Supplementary Fig. 10). We plot the total elastic energy E_{el} as a function of the target angle of the central hinge for the outer
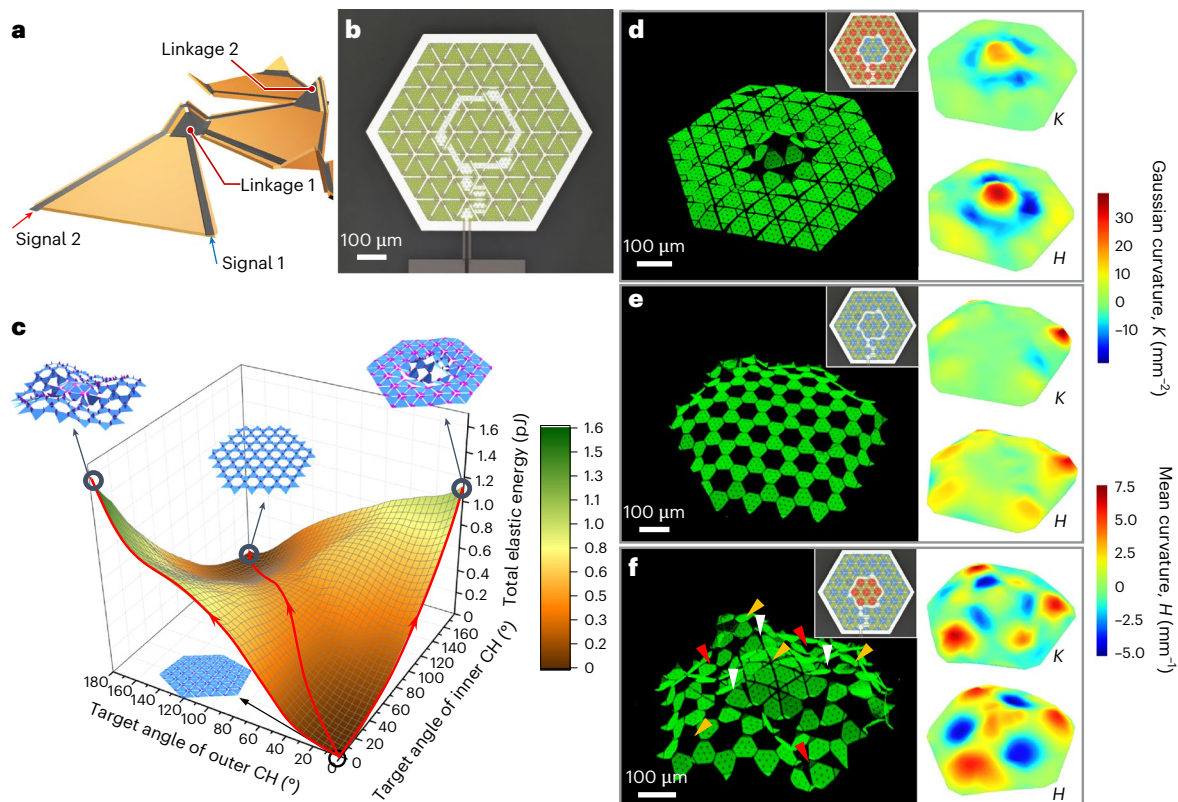
Fig. 3 | Programmable 3D shape shifting from a metabot with multiple actuating regions. a, Schematic of a hinge design with a passive signal wire that can be used to separately address other hinges. In this particular case signal 1 is used to actuate linkage 1 and signal 2 is passed through the first linkage to actuate linkage 2. **b**, An optical image of a fabricated metabot where the interior and exterior parts of the sheet are independently controlled by different electrical signals. **c**, Shape morphing and elastic energy calculations from a simulation of the metabot in a Unity3D engine. Shown is an energy landscape representing the sum of elastic energies corresponding to all of the hinges in the metabot versus the target angles for the outer and inner central hinges (CH). Also shown are the shapes adopted by the simulated sheets at four different points in the parameter space. **d**–**f**, Confocal fluorescence microscopy images of small cap (**d**), plane (**e**) and saddle (**f**) shapes formed from the same pattern with different actuated areas represented by the blue regions in the insets. The corresponding Gaussian (*K*) and mean (*H*) curvatures are plotted on the right.

and inner regions of the sheet in Fig. 3c and Supplementary Figs. 11–14. We find that for actuation pathways associated with simultaneous activation of the inner and outer regions the elastic energy remains relatively small, indicating that the sheet can actuate while maintaining a nearly cylindrically symmetric shape. In contrast, when either the inner or outer regions are actuated independently, the elastic energy is relatively large. This large energy led to formation of frustrated shapes that broke the cylindrical symmetry associated with actuation of a single metasheet unit (Fig. 2a). We find excellent fidelity when comparing these results with the experiments (Fig. 3d–f and Supplementary Video 7). As expected, in regions of the phase space associated with high elastic energy, the sheets adopted a three-fold symmetry associated with higher-order deformation modes (Fig. 3d,f). Specifically, for expansion of the interior linkages with a target of $\lambda = 1.4$ (blue region in the inset of Fig. 3d), the sheet formed a triangular cap with positive curvatures $K \approx 23 \text{ mm}^{-2}$ (Fig. 3d, top right) and $H \approx 7.0 \text{ mm}^{-1}$ (Fig. 3d, bottom right) in the centre of the sheet. Expansion of all the microlinkages yielded a more symmetric planar structure with nearly zero Gaussian and mean curvatures (Fig. 3e, top and bottom right). Finally, when only the outer linkages were expanded, the sheet formed a triangularly symmetric saddle shape (Fig. 3f). Here, the Gaussian curvature (Fig. 3f, top right) had a positive value of $K \approx 25 \text{ mm}^{-2}$ in the centre and at three additional mountain points (orange arrows) and a negative value of $K \approx -12 \text{ mm}^{-2}$ at three saddle points (white arrows). The mean curvature (Fig. 3f, bottom right) had a positive value of $H \approx 5 \text{ mm}^{-1}$ at the mountain points (orange arrows) and a negative value of $H \approx -3 \text{ mm}^{-1}$ at three valley points (red arrows). To show the versatility

of this control strategy, we further divided the metasheet into three or more zones of actuation, which allow for generating more shapes, as shown in Supplementary Video 8. More generally, the full potential of the metasheet in generating a greater variety of shapes could be unleashed if each hinge could be individually controlled by integrating control circuits on each panel rather than sending the signal via electric wires. Collectively, these results demonstrate that separately accessing different regions in the metasheet allows for greater control over the resulting sheet morphology.

Electrically controllable locomoting behaviours

This control can be combined with independent and phase-delayed temporal actuation of two sides of the sheet to generate locomotory gaits in an electrolyte solution as demonstrated in Fig. 4 and Supplementary Video 9. We break the lateral symmetry with either a one-sided brace—the tail—or a more extensive three-sided brace—the head—to yield locomotion via differential shape changes (Fig. 4a). We actuate the metabot using two separate square waves that are phase offset by 90° to generate a four-state machine, where actuating the head primarily lifts the panels off the surface, while actuating the tail primarily extends the length of the sheet in the plane (Fig. 4b). Applying this gait in the experiment produces these four distinct states (Fig. 4c, top): S_0 (head open, tail closed), S_1 (head open, tail open), S_2 (head closed, tail open) and S_3 (head closed, tail closed). We measure a net change in the centre of mass (COM) of the sheet (Fig. 4c, middle), and label each of the four states according to the area expansion of the head and tail panels (Fig. 4c, bottom). As can be seen, our design achieves consistent
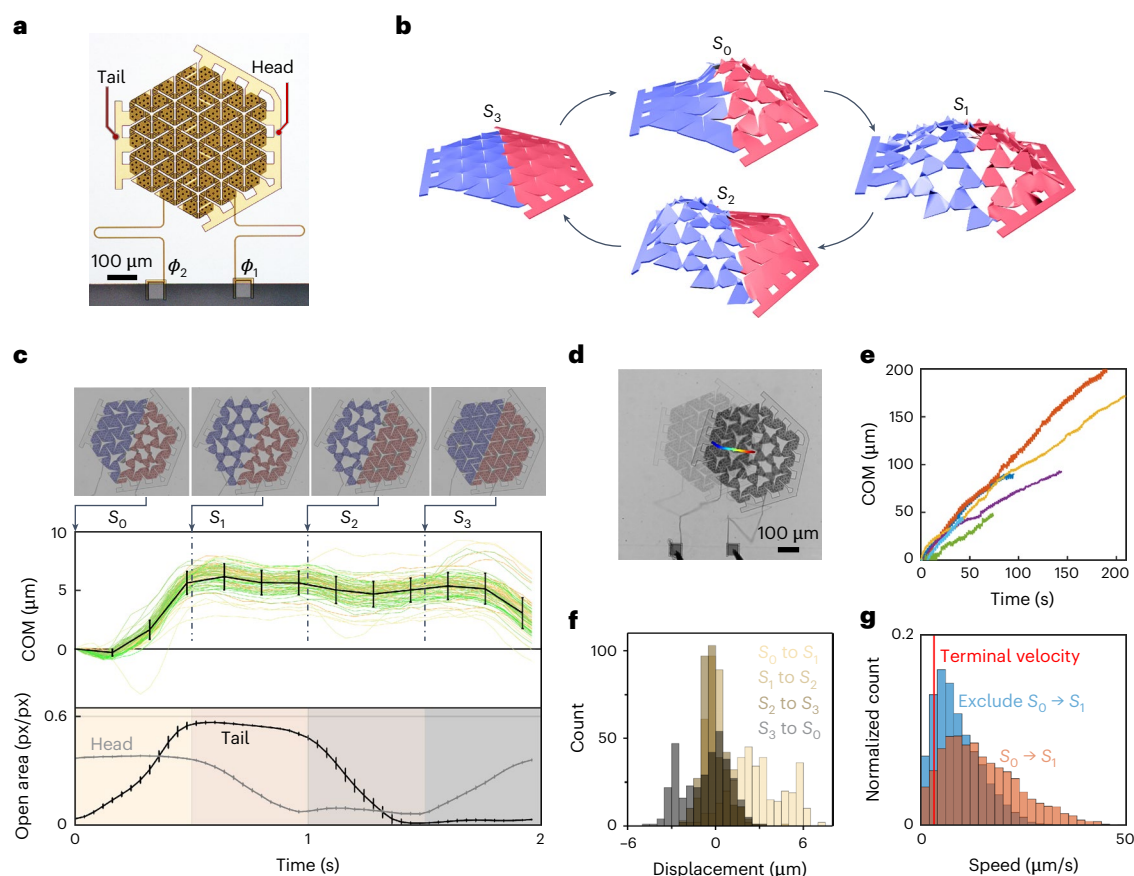
Fig. 4 | Locomoting metabots. a, A micrograph of a sheet where the left and right regions are controlled by separate electrical signals. The right half (head) is braced on three sides while the left half (tail) is braced on a single edge. **b**, A schematic showing cyclic extension–contraction deformations, resulting in a four-state machine. **c**, Actuation cycles associated with actuated patterns. Top: the averaged COM motion for the entire sheet along with false-coloured video frames indicating the sheet configuration at four time points. Bottom: the area expansion ratio for the left and right sides of the sheet. For both COM and open area plots, the centre is the mean, and the error bars are 1 s.d.

The values were calculated over 91 consecutive cycles of the robot. **d**, Overlays of semi-transparent frames along with tracks indicating the COM motions of the individual panels over 190 s. **e**, A plot of the COM of the entire sheet versus time for six different metabots indicates that they locomote at a speed of ~0.9 μm s⁻¹. **f**, A histogram of the displacements between the four states S_0–S_3, indicating that the largest displacement occurs between S_0 and S_1. **g**, A histogram of the instantaneous COM velocities for the sheet. The vertical line indicates estimated terminal velocity due to frictional driving and fluid drag.

locomotion in the direction of the head over many cycles lasting several minutes (Fig. 4d), which we observed across all of six independently tested samples (Fig. 4e), with the greatest displacement occurring when the robot transitions from S_0 to S_1 (Fig. 4f).

Intriguingly, we find evidence that the locomotory mechanism must rely on lubrication forces between the substrate and metabots in solution[32]. Specifically, we rule out friction alone as generating these locomotory gaits. We present a histogram of the instantaneous speed obtained by the sheet in Fig. 4g. For reasonable estimates of the friction coefficient (0.1) and hydrodynamic viscosity, if the entire weight of the robot (~1.4 × 10⁻¹⁰ kg) is put towards locomotion, friction alone could generate only 0.14 nN of force. Assuming that the sheet is a flat disc moving laterally across the substrate in a low-Reynolds-number regime at an effective height of 10 μm, the terminal velocity the sheet could achieve is 3.2 μm s⁻¹ (dashed vertical line in Fig. 4g)[33]. In our experiments, we measure the sheet COM moving at instantaneous speeds of over 50 μm s⁻¹, which is over an order of magnitude larger than the purely frictional terminal velocity (see Supplementary Note for calculation details). Instead, the data indicate that different configurations of the sheet are subject to different lubrication forces opposing the sheet motion. Specifically, expansion and contraction of the tail are coupled with different configurations of the head. When the head is expanded, lubrication forces between the substrate and the metabot

are substantially reduced. As such, when the tail expands (S_0 to S_1), the metabot experiences a large displacement. Conversely, when the head is contracted and flat, the lubrication forces between the substrate and the metabot are relatively high. Thus, when the tail contracts (S_2 to S_3), the metabot undergoes a small displacement. This asymmetry is sufficient to quantitatively explain the collective displacement trends observed in the metabot. The speed of the metabots is determined by both the response time of the microactuators and the locomotory mechanism of the sheet. To enable faster locomotion, it may be necessary to leverage other locomotory mechanisms relying on frictional contacts (see Supplementary Information, Supplementary Fig. 15 and Supplementary Video 10 for more detailed discussion). Importantly, the locomotory modes in these metasheets exhibit more adaptability and robustness to damage than typical legged robots. In Supplementary Fig. 16 and Supplementary Video 11, we show that the metabot could locomote normally even when some of the hinges connecting the panels were severed.

Conclusions
Our ability to design and fabricate microscopic metasheet robots that can adopt a broad range of shapes and achieve locomotion through separate actuation of different regions constitutes a novel paradigm for the design of microscopic robots. While simultaneous actuation

of multiple hinges already enables fascinating locomotory processes, further control over individual hinges, which could be made feasible by integrating electronic circuits on each panel, would unleash the full potential of such metamaterial robots. Such metabots could crawl to a desired location and adopt appropriate conformations that would enhance interfacing with and sensing of, for example, biological tissues and organs. Notably, it was recently shown that the electrochemically actuated hinges driving shape morphing in the metabot can be interfaced with complementary metal–oxide–semiconductor (CMOS) electronics[18,19]. Integration of such circuits into metabots would allow for greater local control and open the door to distributed robotics at the microscale, where the resulting shapes and locomotory behaviours could arise from emergent interactions between the microcircuits. Building metabots with on-board integrated circuits would allow for creation of untethered robots that change their behaviour in response to external optical or radiofrequency commands. Such capabilities would greatly expand the range of environments where the metabots could function. The metamaterial sheet incorporating on-board electronics could build a new form of matter called elastronic metamaterials, where the response could be faster than the speed of sound. Besides the simple locomotion we demonstrated here, these robotic materials would be able to respond in new ways to fluid flows, solid environment and so on. Such capabilities would substantially expand the frontiers of microscale robotics.

Online content

Any methods, additional references, Nature Portfolio reporting summaries, source data, extended data, supplementary information, acknowledgements, peer review information; details of author contributions and competing interests; and statements of data and code availability are available at https://doi.org/10.1038/s41563-024-02007-7.

References

1. Stephens, G. J., Johnson-Kerner, B., Bialek, W. & Ryu, W. S. From modes to movement in the behavior of *Caenorhabditis elegans*. *PLoS ONE* **5**, e13914 (2010).
2. Goldstein, R. E. Green algae as model organisms for biological fluid dynamics. *Annu. Rev. Fluid Mech.* **47**, 343–375 (2015).
3. Mast, S. O. Structure, movement, locomotion, and stimulation in amoeba. *J. Morphol.* **41**, 347–425 (1926).
4. Griniasty, I., Mostajeran, C. & Cohen, I. Multivalued inverse design: multiple surface geometries from one flat sheet. *Phys. Rev. Lett.* **127**, 128001 (2021).
5. Choi, G. P., Dudte, L. H. & Mahadevan, L. Programming shape using kirigami tessellations. *Nat. Mater.* **18**, 999–1004 (2019).
6. Sharon, E., Roman, B., Marder, M., Shin, G. S. & Swinney, H. L. Buckling cascades in free sheets. *Nature* **419**, 579 (2002).
7. Ning, X. et al. Assembly of advanced materials into 3D functional structures by methods inspired by origami and kirigami: a review. *Adv. Mater. Interfaces* **5**, 1800284 (2018).
8. Kim, J., Hanna, J. A., Byun, M., Santangelo, C. D. & Hayward, R. C. Designing responsive buckled surfaces by halftone gel lithography. *Science* **335**, 1201–1205 (2012).
9. Miskin, M. Z. et al. Electronically integrated, mass-manufactured, microscopic robots. *Nature* **584**, 557–561 (2020).
10. Bandari, V. K. et al. A flexible microsystem capable of controlled motion and actuation by wireless power transfer. *Nat. Electron.* **3**, 172–180 (2020).
11. Cui, J. et al. Nanomagnetic encoding of shape-morphing micromachines. *Nature* **575**, 164–168 (2019).
12. Hu, W., Lum, G. Z., Mastrangeli, M. & Sitti, M. Small-scale soft-bodied robot with multimodal locomotion. *Nature* **554**, 81–85 (2018).
13. Jafferis, N. T., Helbling, E. F., Karpelson, M. & Wood, R. J. Untethered flight of an insect-sized flapping-wing microscale aerial vehicle. *Nature* **570**, 491–495 (2019).
14. Wang, J. & Gao, W. Nano/microscale motors: biomedical opportunities and challenges. *ACS Nano* **6**, 5745–5751 (2012).
15. Tanjeem, N., Minnis, M. B., Hayward, R. C. & Shields, C. W. IV Shape-changing particles: from materials design and mechanisms to implementation. *Adv. Mater.* **34**, 2105758 (2022).
16. Li, S. et al. Liquid-induced topological transformations of cellular microstructures. *Nature* **592**, 386–391 (2021).
17. Hines, L., Petersen, K., Lum, G. Z. & Sitti, M. Soft actuators for small-scale robotics. *Adv. Mater.* **29**, 1603483 (2017).
18. Reynolds, M. F. et al. Microscopic robots with onboard digital control. *Sci. Robot.* **7**, eabq2296 (2022).
19. Wang, W. et al. Cilia metasurfaces for electronically programmable microfluidic manipulation. *Nature* **605**, 681–686 (2022).
20. Ren, Z. et al. Soft-robotic ciliated epidermis for reconfigurable coordinated fluid manipulation. *Sci. Adv.* **8**, eabq2345 (2022).
21. Liu, Q. et al. Micrometer-sized electrically programmable shape-memory actuators for low-power microrobotics. *Sci. Robot.* **6**, eabe6663 (2021).
22. Zheng, X. et al. Ultralight, ultrastiff mechanical metamaterials. *Science* **344**, 1373–1377 (2014).
23. Frenzel, T., Kadic, M. & Wegener, M. Three-dimensional mechanical metamaterials with a twist. *Science* **358**, 1072–1074 (2017).
24. Pan, F. et al. 3D pixel mechanical metamaterials. *Adv. Mater.* **31**, 1900548 (2019).
25. Xia, X. et al. Electrochemically reconfigurable architected materials. *Nature* **573**, 205–213 (2019).
26. Tang, Y., Li, Y., Hong, Y., Yang, S. & Yin, J. Programmable active kirigami metasheets with more freedom of actuation. *Proc. Natl Acad. Sci. USA* **116**, 26407–26413 (2019).
27. Peraza Hernandez, E. A., Hartl, D. J. & Lagoudas, D. C. *Active Origami: Modeling, Design, and Applications* (Springer, 2018).
28. Yang, Y., Dias, M. A. & Holmes, D. P. Multistable kirigami for tunable architected materials. *Phys. Rev. Mater.* **2**, 110601 (2018).
29. Peraza Hernandez, E. A., Hartl, D. J. & Lagoudas, D. C. Design and simulation of origami structures with smooth folds. *Proc. R. Soc. A* **473**, 20160716 (2017).
30. Parthasarathy, A., Srinivasan, S., Appleby, A. J. & Martin, C. R. Temperature dependence of the electrode kinetics of oxygen reduction at the platinum/Nafion interface—a microelectrode investigation. *J. Electrochem. Soc.* **139**, 2530 (1992).
31. Park, S. M. et al. Electrochemical reduction of oxygen at platinum electrodes in KOH solutions—temperature and concentration effects. *J. Electrochem. Soc.* **133**, 1641 (1986).
32. Klein, J. et al. Lubrication forces between surfaces bearing polymer brushes. *Macromolecules* **26**, 5552–5560 (1993).
33. Kim, M. U., Kim, K. W., Cho, Y. H. & Kwak, B. M. Hydrodynamic force on a plate near the plane wall. Part I: plate in sliding motion. *Fluid Dyn. Res.* **29**, 137–170 (2001).

Methods

Fabrication of metabots

The fabrication process relies on growing sacrificial layers, fabricating rigid panels, patterning SEAs and finally releasing the resulting structures. (1) To fabricate the release layers, we thermally evaporated 180 nm aluminium and deposited 30 nm of Al_2O_3 using atomic layer deposition at 110 °C sequentially on a fused silica wafer. The sacrificial layers were then patterned photolithographically and were etched using aluminium etchant at 50 °C. (2) To fabricate the rigid panels, a 550-nm-thick silicon dioxide or silicon nitride layer was deposited using plasma-enhanced chemical vapour deposition (Oxford 100). A positive photoresist (MICROPOSIT S1813) was spin-coated and patterned. The silicon dioxide or silicon nitride layer was then etched with CHF_3/O_2 at 240 W using inductively coupled plasma etching (Oxford PlasmaLab 80+). (3) To pattern the bottom titanium layer, a negative photoresist (NLOF 2020) was spin-coated and patterned. A 2 nm layer of Ti was sputtered onto the sample at 3 mTorr and 400 W. Any Ti deposited on the photoresist was removed using a lift-off process, leaving a patterned Ti layer on the substrate. (4) Next, we patterned the platinum layer. We grew 7 nm of Pt onto the Ti using atomic layer deposition. A positive photoresist (MICROPOSIT S1805) was spin-coated, and the pattern was defined photolithographically. The Pt was then etched with an ion mill and we removed the photoresist using an organic solvent. Platinum is also used to make the conductive wires that transmit the control signal. We did not observe ruptures of the wires and actuators owing to the strong adhesion of atomic-layer-deposited platinum and the rigid panels. (5) Finally, we patterned the top titanium layer. A negative photoresist (NLOF 2020) was spin-coated and patterned. A second 2 nm layer of Ti was sputtered onto the sample at 3 mTorr and 400 W. The sputtered Ti on top of the photoresist was lifted off in solvent, leaving a patterned Ti layer on the substrate.

The devices were then immersed in AZ 726 MIF basic developer containing 2.38% tetramethylammonium hydroxide for several hours to etch the aluminium and Al_2O_3 sacrificial layers, thereby releasing the devices into the solution. The devices were then washed using deionized water several times and transferred into 1× PBS solution. The schematics of the metabots and the fabrication of a metabot are shown in Supplementary Fig. 1.

Electron microscopy imaging

To obtain the SEM images of the devices (Fig. 1), the samples were released from the substrate and washed using deionized water and isopropanol sequentially. Then, the samples were dried in a critical-point drier (Leica CPD300), sputtered with a thin layer of gold and imaged using SEM (Zeiss Supra 55).

Electric actuation of metabots

Electric actuation of metabots was performed in a custom-built two-electrode electrochemical cell on an inverted microscope (Olympus IX71) integrated with a three-axis micromanipulator (Sensapex) and video camera. Each metabot acted as the working electrode. A PtIr probe coated with parylene C (Microprobes for Life Science) was used to connect a function generator to the metabots. The reference electrode was a commercial flexible Ag/AgCl electrode in 3 M KCl (FLEX-REF, World Precision Instruments) with a low electrolyte leakage. Cyclic voltammetry was performed using the following approach: a sweep voltage was generated via a data acquisition board controlled using a LabVIEW program, and the current was amplified through a current amplifier and collected by the same data acquisition board. These experiments were conducted in 1× PBS (pH 7.45). All the potential values in this study are specified relative to the Ag/AgCl/3 M KCl reference electrode used. The cyclic voltammetry data were taken at a sweep rate of 1 V s⁻¹. The optical images were taken using a monochromatic camera mounted on the microscope.

Addressable control of metabots

The 7-nm-thick platinum layer functions dually as the active layer in the microactuators and as the conductor. Synchronization of microactuators within the same zone is achieved through the Pt layer on the panel and the Pt wire via the hinge mechanism. Electric signals are directed to the microactuators in various regions from the electrodes by routing platinum wires through hinges (Supplementary Fig. 8). A function generator equipped with multiple outputs and programmable phase shift capability is connected to the electrodes, delivering a controllable voltage relative to the Ag/AgCl reference electrode. The bending curvature of microactuators is precisely regulated by adjusting the applied voltages, as detailed in our previous research.

The sheet resistance of the 7-nm-thick platinum measures 15.8 Ω sq⁻¹. Considering a typical length-to-width ratio of the platinum layer ranging from 1 to 20, the sheet resistance falls within the range of 16–320 Ω sq⁻¹. The average Faraday resistance of the platinum actuator throughout an entire redox cycle is approximately 10^3 Ω cm². In a zone containing 100 actuators and with a total platinum area of about 10^3 μm², the combined Faraday resistance of the actuators totals 10^4 Ω. The platinum wire exhibits a resistance two orders of magnitude lower than the Faraday resistance of the platinum actuators. Hence, the Pt layer can serve both as an active layer of the microactuators and a conducting layer, and can synchronize the signals across each actuator within the same zone, enabling simultaneous control of the actuators.

3D optical imaging

3D optical imaging was carried out using a set-up consisting of a micromanipulator, a reference electrode and a function generator built around a confocal microscope LSM710 (Zeiss). For confocal fluorescence microscopy imaging, we labelled the rigid panels of metabots with the fluorescent dye Alexa Fluor 405 NHS ester via a silane agent, (3-aminopropyl)triethoxysilane[1]. The excitation laser wavelength was 405 nm and the fluorescence with wavelength between 425 and 600 nm was collected. A 40× water-immersion objective with a high numerical aperture of 1.1 was used for imaging. The 3D images were reconstructed using ImageJ 3D Viewer.

Data availability

Source data are provided with this paper. Additional data are available from the corresponding authors upon request.

Author contributions

Q.L., A.B.A., N.L.A., H.K.-G., P.L.M. and I.C. conceived the project. Q.L. and W.W. performed the pattern design and device fabrication. Q.L. performed the SEM imaging, confocal fluorescence microscopy imaging, electrochemical measurements and shape morphing experiments. Q.L. and W.W. conducted the locomotion experiments. H.S., I.G., Q.L. and H.K.-G. performed the simulation. J.T.P., Q.L. and I.G.

Competing interests

Q.L., P.L.M. and I.C. are inventors on a patent application (PCT/US2021/021419) submitted by Cornell University that covers electrically programmable microscale shape-memory actuators and related robotic devices. W.W., Q.L., M.F.R., P.L.M. and I.C. are inventors on a provisional patent application (63/267,190) submitted by Cornell University that covers actuators and control electronics for cilium metasurfaces and a provisional patent application (63/368,751) submitted by Cornell University that covers integrated circuits for controlling microscopic robots. The other authors declare no competing interests.

Additional information

Supplementary information The online version contains supplementary material available at https://doi.org/10.1038/s41563-024-02007-7.

Correspondence and requests for materials should be addressed to Itai Cohen.

Peer review information *Nature Materials* thanks Sung Kang, Metin Sitti and Jie Yin for their contribution to the peer review of this work.

Reprints and permissions information is available at www.nature.com/reprints.